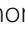


FULL PAPER

Open Access



Overview of Akatsuki data products: definition of data levels, method and accuracy of geometric correction

Kazunori Ogohara^{1*} , Masahiro Takagi², Shin-ya Murakami³, Takeshi Horinouchi⁴, Manabu Yamada⁵, Toru Kouyama⁶, George L. Hashimoto⁷, Takeshi Imamura⁸, Yukio Yamamoto⁹, Hiroki Kashimura¹⁰, Naru Hirata¹¹, Naoki Sato¹², Atsushi Yamazaki³, Takehiko Satoh³, Naomoto Iwagami²⁰, Makoto Taguchi¹³, Shigeto Watanabe¹⁴, Takao M. Sato³, Shoko Ohtsuki¹⁵, Tetsuya Fukuhara¹³, Masahiko Futaguchi¹⁶, Takeshi Sakanoi¹⁷, Shingo Kameda¹³, Ko-ichiro Sugiyama¹⁸, Hiroki Ando¹⁹, Yeon Joo Lee³, Masato Nakamura³, Makoto Suzuki³, Chikako Hirose³, Nobuaki Ishii³ and Takumi Abe³

Abstract

We provide an overview of data products from observations by the Japanese Venus Climate Orbiter, Akatsuki, and describe the definition and content of each data-processing level. Levels 1 and 2 consist of non-calibrated and calibrated radiance (or brightness temperature), respectively, as well as geometry information (e.g., illumination angles). Level 3 data are global-grid data in the regular longitude–latitude coordinate system, produced from the contents of Level 2. Non-negligible errors in navigational data and instrumental alignment can result in serious errors in the geometry calculations. Such errors cause mismapping of the data and lead to inconsistencies between radiances and illumination angles, along with errors in cloud-motion vectors. Thus, we carefully correct the boresight pointing of each camera by fitting an ellipse to the observed Venusian limb to provide improved longitude–latitude maps for Level 3 products, if possible. The accuracy of the pointing correction is also estimated statistically by simulating observed limb distributions. The results show that our algorithm successfully corrects instrumental pointing and will enable a variety of studies on the Venusian atmosphere using Akatsuki data.

Keywords: Venus, Data product, Pointing correction, Ellipse-fitting technique

Introduction

The Venus Climate Orbiter, Akatsuki, is a Venus weather satellite launched on May 21, 2010 (Nakamura et al. 2011, 2016). The Akatsuki mission observes cloud distributions at several altitudes on both the dayside and nightside over five wavelength regions selected to obtain cloud distributions at different altitudes. Its main scientific purpose is to contribute to the understanding of the atmospheric circulation and cloud formation processes of Venus. To obtain meteorological information, global

three-dimensional maps of the clouds are taken by four cameras at ultraviolet and infrared wavelengths; lightning is detected by a high-speed imager, and vertical atmospheric structures are observed by a radio-occultation technique. Since Akatsuki is in an equatorial elongated orbit with a period of about 11 Earth days, complementary to the polar orbit of Venus Express, which had a period of an Earth day, cloud motions and/or temporal variations at altitudes of about 45–70 km can be well observed continuously over a long period. Systematic imaging observations by Akatsuki are widely expected to enable the three-dimensional visualization of Venusian atmospheric dynamics. In this paper, useful information about the Akatsuki data products is presented.

*Correspondence: ogohara.k@e.usp.ac.jp

¹ School of Engineering, University of Shiga Prefecture, 2500, Hassaka, Hikone, Shiga 522-8533, Japan

Full list of author information is available at the end of the article

The atmospheric super-rotation of Venus is one of the most remarkable phenomena in planetary science. Venusian rotation is very slow, having a period of about 243 Earth days, such that an axisymmetric subsolar-to-antisolar (SS-AS) circulation was expected to be predominant (e.g., Stone 1968; Dickinson 1969). However, a number of observations have shown that a fast zonal wind is predominant in the Venusian atmosphere below ~ 80 km altitude (e.g., Schubert 1983). Almost the entire atmosphere of Venus rotates much faster than Venus itself; the zonal wind increases almost linearly with altitude from the ground and reaches about 100 m s^{-1} at the cloud's top level (~ 70 km altitude), which is about 60 times faster than Venus's solid globe. To explain the generation and maintenance mechanism of the Venusian atmospheric super-rotation, several mechanisms based on thermal tides, meridional circulation, or SS-AS circulation have been proposed (Schubert and Whitehead 1969; Thompson 1970; Fels and Lindzen 1974; Gierasch 1975; Matsuda 1980). Recent numerical studies suggest that both the thermal tide (e.g., Takagi and Matsuda 2006, 2007) and meridional circulation mechanisms (e.g., Yamamoto and Takahashi 2004) might be viable in the Venusian atmosphere, in which the vertical and horizontal transport of angular momentum due to thermal tides, eddies, and mean meridional circulation plays an important role. Other kinds of waves, such as the four- and five-day waves found in UV images of the cloud top (e.g., Del Genio and Rossow 1990; Kouyama et al. 2013, 2015) and small-scale disturbances suspected to be related to gravity waves (e.g., Sagdeev et al. 1986; Hinson and Jenkins 1995; Peralta et al. 2008; Garcia et al. 2009) may also play important roles in the establishment and maintenance of the atmosphere's super-rotation. Schubert et al. (1980) suggested that the zonal-mean meridional circulation consists of several vertically stacked cells extending from the equator to poles, based on wind profiles obtained by entry probes. Significant poleward winds at the cloud-top level have been observed in previous observations (e.g., Machado et al. 2017). It is noted, however, that the number of observed regions and/or local times has been limited and that the horizontal winds observed at the cloud top may include those associated with the thermal tide and various waves. We have no observational results as yet for the *zonally averaged* meridional circulation in the Venusian atmosphere. To elucidate the dynamical effects of meridional circulation, waves, and eddies, their three-dimensional structures on both the dayside and nightside must be understood (Peralta et al. 2008).

The clouds, which result in a ~ 0.76 integrated-bond albedo for the planet (Moroz et al. 1985), play a major role in controlling the energy balance of the atmosphere. Sulfuric acid cloud particles are produced through

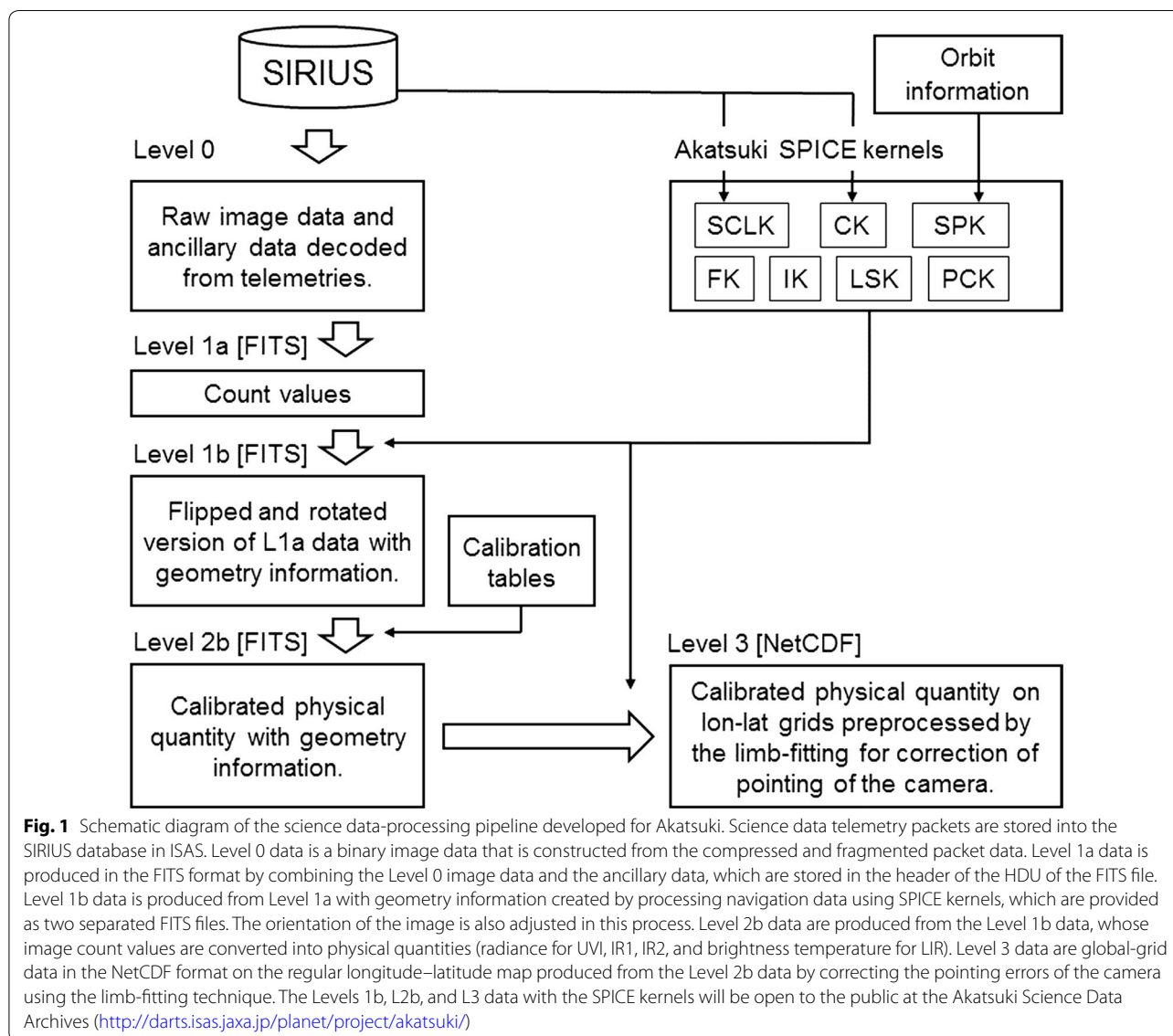
photochemistry near and above the cloud tops and through condensation in updrafts within the clouds (Krasnopolsky and Pollack 1994; Imamura and Hashimoto 2001); however, specific dynamical processes contributing to the transport of key species such as SO_2 and cloud droplets are unclear. Moreover, there is an unidentified ultraviolet absorber in the clouds, which causes dark features in the UV, with related localized decrease in the albedo. This shows spatial and temporal variations, but its cause is unknown (Lee et al. 2015). To better understand the climate system of the cloudy planet, simultaneous global monitoring of the clouds' optical properties and the three-dimensional wind fields in various spatial scales is essential.

Atmospheric motion can be derived from cloud motions using cloud-tracking techniques (e.g., Rossow et al. 1990). It is difficult, however, to obtain the cloud-motion vectors (CMVs) accurately because the Venus disk on the detector array changes with time in the field of view (FOV). Uncertainties in the spacecraft attitude, the alignment of the instruments, and the like are also problematic. To derive the atmospheric motions accurately, it is crucially important to reduce attitudinal errors in the spacecraft and correct geometry coordinate information such as latitude and longitude. Since three-dimensional atmospheric motions can be complex, it is important to easily link and compare data at various altitudes obtained by different cameras and/or at different wavelengths. To realize this kind of data analysis, a data-archive design that enables users to treat data without any gaps between scientific instruments is required. It is also important to employ conventional analytical methods in terrestrial atmospheric science for direct and efficient application to the Akatsuki data. We have considered an appropriate format for the Akatsuki data, keeping in mind that the data would become a common heritage of humankind, just as previous planetary-exploration data have become.

In this paper, we present the data-processing schemes, content, and format of the Akatsuki public data in "Definition of data levels" section. We describe the method used to reduce the errors in spacecraft attitude and correct the geometry information, an improved limb-fitting technique originally described by Ogohara et al. (2012), in "Reliability of pointing correction by limb fitting" section. We also provide initial quality and accuracy estimations, which will be useful in the analysis of Akatsuki data in "Reliability of pointing correction by limb fitting" section. "Summary" section is a summary of this paper.

Definition of data levels

Akatsuki image data obtained by four imaging cameras (IR1, IR2, LIR, and UVI) are processed by a common data-production pipeline (Fig. 1). This pipeline is roughly



divided into four levels (Levels 0–3), because returning to raw data is not necessary, for example, when calibration and geometry-correction techniques are improved. Table 1 summarizes the standard and ancillary data products of the four imaging cameras. Levels 1, 2, and 3 and the auxiliary data products (which will be defined in the following subsections) will be open to the public about 1.5 years after the arrival of the image data at the Akatsuki Science Data Archives (<http://darts.isas.jaxa.jp/planet/project/akatsuki/>). In addition to such image products, documents of the directory tree and the header list will be released to the public through the archive site (e.g., for L2b of UVI, http://darts.isas.jaxa.jp/pub/pds3/vco-v-uvi-3-cdr-v1.0/vcouvi_1001/document/).

Level 0

Level-0 (L0) image data are the uncalibrated count values (i.e., not directly related to physical quantities) of each imaging camera, produced from raw telemetry. Ancillary data contain meta-data about the image (e.g., time of observation and exposure time duration) that are also produced from raw telemetry and ranging data.

Level 1

Level-1 data also consist of uncalibrated count values and are divided into two datasets. Level-1a (L1a) image data are produced in the FITS format by combining the Level-0 (L0) image data and the ancillary data, some of which are stored in the header of the HDU (Header Data

Table 1 Definitions of the Akatsuki data-processing levels

Abbr.	Level	Description
L0	Level 0	Raw data
L1a	Level 1a	Count values in FITS format
L1b	Level 1b	Flipped and rotated version of L1a with summary of geometry information in FITS format, and detailed geometry information in FITS format
L2b	Level 2b	Calibrated physical quantity with geometry information in FITS format
L3	Level 3	Calibrated physical quantity on longitude–latitude grids in NetCDF format which is preprocessed using the limb-fitting technique for pointing correction of the camera, including corrected geometry information

Definitions of the Akatsuki data-processing levels, which are common in UVI, IR1, IR2, and LIR instruments. The L1b, L2b, and L3 data products will be open to the public at the Akatsuki Science Data Archive (<http://darts.isas.jaxa.jp/planet/project/akatsuki/>)

Unit) of the L1a FITS file, e.g., observation-program ID, exposure time, filter name, housekeeping data, and observational information such as time indicators (TIs).

Level-1b (L1b) image data are produced from L1a data as two geometry information files are created by processing navigational data in the SPICE-kernel format using the SPICE toolkit. The SPICE kernels related to Akatsuki are summarized in a meta-kernel file (e.g., `vco_v01.tm`) provided at the Akatsuki Science Data Archive. The ancillary data including observation date, instrument name, and filter name are stored in the header of the HDU of the L1b FITS file. A complete dictionary of the FITS header keywords stored in the L1b (and also L2b in the following subsection) FITS files is also present in the Akatsuki Science Data Archives. The geometry data are composed of multiple two-dimensional arrays, such as images observed, and include Venus longitude, latitude, local (solar) time, solar-incidence angle, emission angle, azimuthal angle (angle between the projection of the incidence and emission vectors onto the cloud-layer surface), and phase angle. One geometry file (geo file) includes the geometry data at the center of each pixel, and the other file (geo4 file) includes information at each pixel limit. The orientation of the image data is adjusted during this L1a-to-L1b processing by a procedure that combines 90° rotation and vertical flipping of the image. In the L1b-image data, the + Y-axis of the spacecraft (+ Y_{SC}), which is aligned with the solar-cell paddles, runs from the bottom of the image to the top (Ishii et al. 2004). This procedure differs among the cameras and filters because the alignment of each instrument against the spacecraft differs. The operated orientation adjustment is recorded as a value of the `P_FLPROT` keyword in the header of the HDU in the FITS file. To allow a quick look, a JPEG image is created for each FITS image file. See the catalog files provided in the public data for more details.

Level 2

Level-2 image data are produced from the L1b data (image data and geometry information), whose image

count values are converted into physical quantities—namely, the radiation flux (for IR1, IR2, and UVI) and brightness temperature (for LIR), which have been calibrated by laboratory data and/or particular observations conducted for IR1 and UVI. For a quick look, JPEG images are also created for each FITS image file. Hereafter, we refer to Level 2 as Level 2b (L2b) to explicitly show the source data are L1b. It should be noted that Level 2a (L2a), which is L1a calibrated, is not produced because the calibrated L2b data are adequate for scientific research.

L2b image data share a FITS file format with L1b, which is fully compliant with the FITS Standard Version 4.0 [DRAFT] published online on July 22, 2016, by the IAUFWG. The image data are stored in the data part of the secondary HDU as an IMAGE extension. In all data stored in the HDU, + Y_{SC} is upward and the – Z-axis of the spacecraft (– Z_{SC}) is rightward; when using the common coordinate system with the origin at the lower-left corner of the image, the horizontal axis (the first axis) is oriented from left to right, and the vertical axis (the second axis) is oriented from bottom to top. This coordinate system is commonly used in visualization software for FITS files, such as SAOImage DS9.

Each value in the L1b and L2b data arrays represents a value at the center of a pixel. The following three types of special pixels are defined. The first are missing pixels, which represent missing telemetry due to packet loss or override by other data in the data recorder (DR). The second are dead pixels, representing pixels that have been permanently damaged through such phenomena as X-ray hits to the corresponding detector element. The third are saturated pixels, representing data points that fall outside the nominal measurement range due to too many photons being received at the detector element. These three special pixels are defined and recorded in the header of the HDU in the FITS file using the following keywords `P_MPIXV` (missing pixel flag value), `P_DPIXV` (dead pixel flag value), `P_SPIXV` (saturated pixel flag value), and `P_SPIXO` (saturated pixel offset value). For completeness,

the following keywords are also defined in the header of HDU: P_MPIXN (the number of missing pixels), P_DPIXN (the number of dead pixels), and P_SPIXN (the number of saturated pixels). For more details, see the catalog file (dataset.cat) provided in the Akatsuki dataset.

The geometry data included in the L1b- and L2b-image data are calculated using the VCO SPICE-kernel dataset, which is available from DARTS for ISAS/JAXA and from the PDS SPICE Archives at JPL/NASA. It should be emphasized that the geometry calculations are performed by assuming specific altitudes: 70 km for the UVI 283- and 365-nm channels, as well as the IR2 2.02- μm channel, 60 km for the IR1 0.90- (dayside), 0.90- (nightside), 0.97-, and 1.01- μm channels, 65 km for the LIR pic channel,¹ and 50 km for the IR2 1.735-, 2.26-, and 2.32- μm channels. The assumed altitude is recorded in the FITS file header under the keyword S_CLDALT. Some of the geometric quantities appearing in the labels and headers of the FITS files are in J2000 coordinates. For the Venusian geometry, IAU_VENUS, which is defined as the planetocentric coordinate system for Venus, is used.

Level-3 data

One of the remarkable advantages of Akatsuki is that it allows continuous global monitoring from an equatorial orbit. Using sequential global images, we can visualize the propagation of atmospheric waves and estimate atmospheric motion by measuring the displacement of cloud features on images over a time interval Δt . This traditional method is applicable to all cameras and filters except for LAC. However, it is difficult to track a cloud feature and to measure its displacement in meters because the size and position of the Venus disk temporally vary in the FOV. Data analyses, such as an estimation of the phase speed of atmospheric waves, also suffer from the same difficulty. To promote a variety of scientific studies, we provide Level-3 (L3) data, in which observed variables are mapped onto a regular (equi-spaced) longitude–latitude grid. L3 data are produced from the L2b image data and are distributed in the Network Common Data Form (NetCDF) file format, which is widely used in the atmospheric science community and simplifies the application of conventional analytical methods to the Akatsuki image data. The resolution of the L3 longitude–latitude map is fixed at $0.125^\circ \times 0.125^\circ$ (2880×1440 grids for 360° longitude and 180° latitude) for all image data obtained from our four image cameras.

Figure 2 shows a sample of longitude–latitude images generated using the SPICE toolkit and kernels (<https://naif.jpl.nasa.gov/naif/toolkit.html>). The dark area around

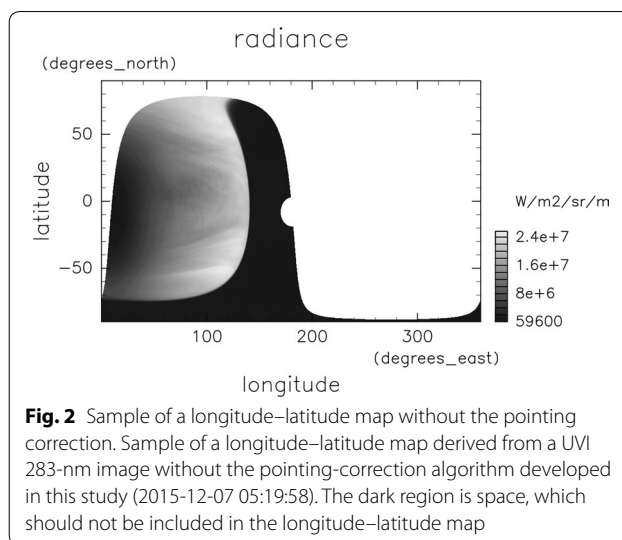
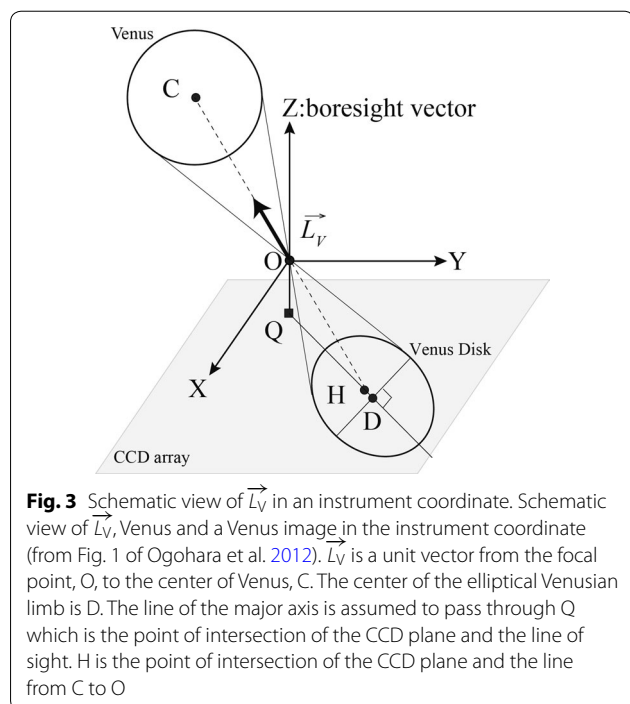


Fig. 2 Sample of a longitude–latitude map without the pointing correction. Sample of a longitude–latitude map derived from a UVI 283-nm image without the pointing-correction algorithm developed in this study (2015-12-07 05:19:58). The dark region is space, which should not be included in the longitude–latitude map

the Venus limb is an area outside of the disk of Venus (i.e., in space) on the L2 image but is recognized as being inside the Venus disk based on the SPICE kernels. This type of mismapping results from errors in instrumental pointing associated with the attitude of the spacecraft and the alignment of the instruments. Although errors in the alignment of instruments can be reduced by stellar observations, errors in the spacecraft attitude still remain. Since the attitude determination accuracy is around 0.01° (1.75×10^{-4} rad) or worse (Nakamura et al. 2011), the positions of cloud patterns in L2b images fluctuate by more than a pixel due to errors in the attitude of the spacecraft (Ogohara et al. 2012). Assuming $\Delta t = 2$ h, a positional error of 1 pixel leads to errors of $3\text{--}10 \text{ m s}^{-1}$ in cloud speed, depending on the distance of the spacecraft from the center of Venus and the instantaneous field of view (IFOV) of the instruments. An error of a few meters per second in speed may be negligible compared to super-rotation; however, considering that 1 pixel is the ideal cloud-position error in an image with high accuracy in attitude determination, it cannot be ignored in comparison with the meridional component and the disturbances of the CMVs.

Such pointing errors in cameras can be corrected by calculating the position vector of Venus's center, \vec{L}_V , in instrumental coordinates (Fig. 3). The Venus disk is imaged as an ellipse. Because the spacecraft–Venus-center distance, the wavelength-dependent cloud altitude, and the IFOV can be assumed to be known, \vec{L}_V can be uniquely determined if the positions of D and the semimajor axis of the elliptical Venus disk in Fig. 3 are determined by limb fitting (see Ogohara et al. 2012 for details). Therefore, an accurate determination of the Venusian limb on an image is required to accurately

¹ A 60-km altitude is assumed for the LIR pic channel in the dataset used in this study (internal release version v20170601).



convert an L2 image into a longitude–latitude map. Ogohara et al. (2012) showed that such a method of pointing correction offered a sufficiently high accuracy for Venusian atmospheric science using UV images taken by the Venus Monitoring Camera onboard Venus Express (VMC/Venus Express). The pointing-correction accuracy of multi-wavelength Venusian images taken by Akatsuki is estimated in “Reliability of pointing correction by limb fitting” section.

L3 data include observed variables (i.e., radiance or brightness temperature) and geometry data (i.e., incidence, emission, phase, and azimuthal angles) calculated based on corrected pointing information determined by the ellipse-fitting technique (Fig. 4). The contents of the L3 data are summarized in Table 2. The assumed cloud altitudes are identical to those described in the L2 data, which depend upon wavelength. The horizontal resolution is $0.125^\circ \times 0.125^\circ$ (2880×1440 grids), as described above. Each grid interval on the equator is approximately 13 km, which is comparable to the spatial resolution around the sub-spacecraft point in L2 images other than LIR, when the distance of the spacecraft from Venus’s center is roughly 7×10^4 km. To verify the results of limb detection and limb fitting, Level 3x (L3x) NetCDF and FITS files are also created. The L3x FITS file has a similar structure to the geometry information (geo) file generated at the same time as L1b, so the L3x FITS file can be

used as a pointing-corrected geometry information file instead of the normal geometry information file.

Reliability of pointing correction by limb fitting

In this section, the accuracies of the limb fitting and pointing correction are evaluated by simulating the Venusian limb observed by the cameras (Ogohara et al. 2012). A few updates on the limb-fitting algorithm from Ogohara et al. (2012) are described in the following subsection. To simulate the Venusian limb, the shape of the Venusian limb observed by cameras was investigated, revealing that the limb could not be approximated by an ellipse plus random noise, as was done by Ogohara et al. (2012) for the VMC-UV images of Venus. Thus, the method used for simulating the Venusian limb observed by Akatsuki, rather than VMC, is reported. The artificial elliptical limbs are then randomly generated, using our method, and the accuracy in the pointing correction is evaluated by fitting ellipses to the artificial limbs.

Method of limb fitting

The ellipse-fitting technique used in this study is an improved version of the method that Ogohara et al. (2012) developed for UV images taken by VMC. There are two points of difference. First, limb points used for ellipse fitting are detected by fitting the hyperbolic tangent (tanh) function to one-dimensional radiance distributions in the X - or Y -directions, whereas the limb points were detected by Ogohara et al. (2012) using a combination of linear and tanh functions (referred to as the x tanh function, hereafter). This change was made because we empirically confirmed that the misfitting rate is lower and the variance of detected limb points is smaller in the tanh cases than in the x tanh cases for the Akatsuki data. The use of tanh fitting for limb-point detection contributes to the increase in limb points, especially in nightside images with low contrast between space and the Venusian disk. Moreover, we also changed the optimization algorithm. Ogohara et al. (2012) adopted a method in which an ellipse was updated step by step using multiple optimization algorithms, starting with the optimization algorithm presented by Taubin (1991) in the first step. However, some VMC-UV images clearly show incorrect elliptical results. In such cases, we adopt the HLS method (Iwamoto et al. 2009), instead of the Taubin method, to improve the ellipse fitting, since we found that the HLS method is more robust than the Taubin method when applied to Akatsuki images. The above two modifications did not decrease the accuracy of the elliptical fitting or pointing correction as long as VMC-UV images were used.

Simulating limb-point distributions for accuracy estimation

Although Ogohara et al. (2012) presented the accuracy of the ellipse fitting and pointing correction for VMC-UV images, the correction accuracy may depend upon cameras and wavelengths. In particular, the accuracy for an image of Venus’s nightside taken by Akatsuki’s IR2 camera may not be as high as that for VMC-UV images. Hence, we simulate the typical Venusian limb observed by the four cameras onboard Akatsuki, as Ogohara et al. (2012) did, and estimate the accuracy of the pointing correction.

Letting (p_{xi}, p_{yi}) be the position of the i th limb point ($1 \leq i \leq M$), we define the argument of this point, θ_i , as follows:

$$\theta_i = \tan^{-1} \frac{p_{yi} - y_c}{p_{xi} - x_c} \tag{1}$$

Here, (x_c, y_c) is the position of the ellipse’s center determined by fitting an ellipse to M limb points. The defined range of θ_i is $(-90^\circ, 90^\circ)$ for $p_{xi} > x_c$ and $(90^\circ, 270^\circ)$ for

Table 2 Major variables stored in the L3 NetCDF file

Variable	Description
Longitude	Longitudes of the map grid (degrees_east)
Latitude	Latitudes of the map grid (degrees_north)
Time	Observation time (hours since 2000-1-1 00:00:00: UTC)
Radiance/btemp	Radiance (UVI, IR1, IR2)/brightness temperature (LIR)
inangle	Incidence angles
emangle	Emission angles
phangle	Phase angles
azangle	Azimuthal angles
FIT_STAT	Limb-fitting status: - 1 (not used), 0 (NG), 1 (OK), and 2 (OK but inaccurate)
D_SSCPX	Corrected sub-spacecraft position on L2b image (axis1)
D_SSCPY	Corrected sub-spacecraft position on L2b image (axis2)
D_NPVAZM	Corrected S_NPVAZM
D_LVANG	Rotation angle of the line-of-sight (LOS) vector determined by the limb fitting

Other variables inherited from the L2b FITS data are also stored. See the header information of the L3 NetCDF file by the ncdump command for more details

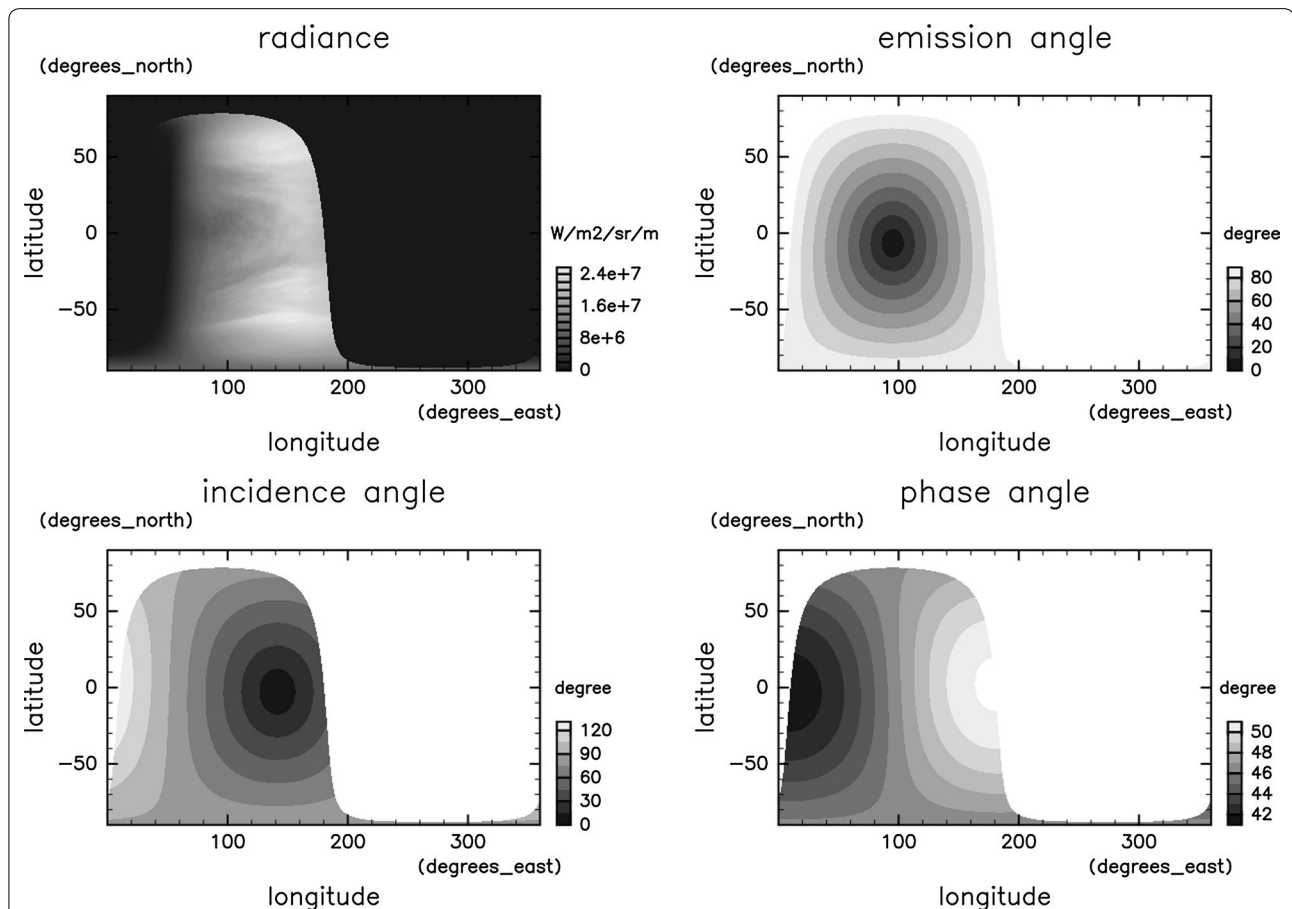


Fig. 4 Sample of the Level 3 product. Sample of the Level 3 data of UVI 283 nm (2015-12-07 05:19:58), which include longitude–latitude maps of radiance, emission, incidence, phase, and azimuthal angles. In the case of LIR, brightness temperature instead of radiance is included in Level 3 data

$p_{xi} < x_c$. Furthermore, the radial residual between the i th limb point and the ellipse, $r(\theta_i)$, is defined as

$$r(\theta_i) = \sqrt{(p_{xi} - x_c)^2 + (p_{yi} - y_c)^2} - \sqrt{(x - x_c)^2 + (y - y_c)^2}, \quad (2)$$

$$\frac{y - y_c}{x - x_c} = \tan \theta_i, \quad (3)$$

where (x, y) is a point on the ellipse. Figure 5 shows images observed by the four cameras and the radial residuals, r , obtained by applying ellipse fitting to them. The radial-residual distribution in the 283-nm images (Fig. 5h) appears to have a “3” shape, and in contrast, that in the 2.02- μm images (Fig. 5d) seems to have an “ ε ” shape with a phase opposite to the 3-shape. The limb points in the LIR image (Fig. 5f) are successfully detected at most arguments, and the distribution of their radial residuals from the ellipse is smooth. Although the 3-shape is also seen in the nightside image (1.01 μm , Fig. 5b), the limb points are distributed widely around the 3-shape due to the low contrast between the Venusian disk and space. Ogohara et al. (2012) investigated the accuracy of the ellipse fitting, assuming that the positions of the limb points detected in Venusian images could be simulated by adding Gaussian noise to a true ellipse. Their assumption was realistic as far as they used VMC-UV images; however, it is obviously unrealistic in the case of images taken by Akatsuki because they did not consider the 3-shape or the ε -shape of the radial residuals shown in Fig. 5. We generate limb-point distributions randomly by adding Gaussian noise to a distribution of r that can be approximated by polynomials such as the 3-shape and ε -shape, fit an ellipse to the limb points, and investigate variations in the sub-spacecraft points in images determined by ellipse fitting.

Based on the 1.01- μm , 2.02- μm , LIR, and 283-nm images shown in Fig. 5, r can be expressed as the summation of the noise and a sixth-order polynomial function of argument θ as follows:

$$r(\theta) = a\theta^6 + b\theta^5 + c\theta^4 + d\theta^3 + e\theta^2 + f\theta + g. \quad (4)$$

Here, θ is defined in the range of $[-90, 270)$, because the limb located on the right-hand side of an image becomes discontinuous. Solid lines shown in Fig. 5 are

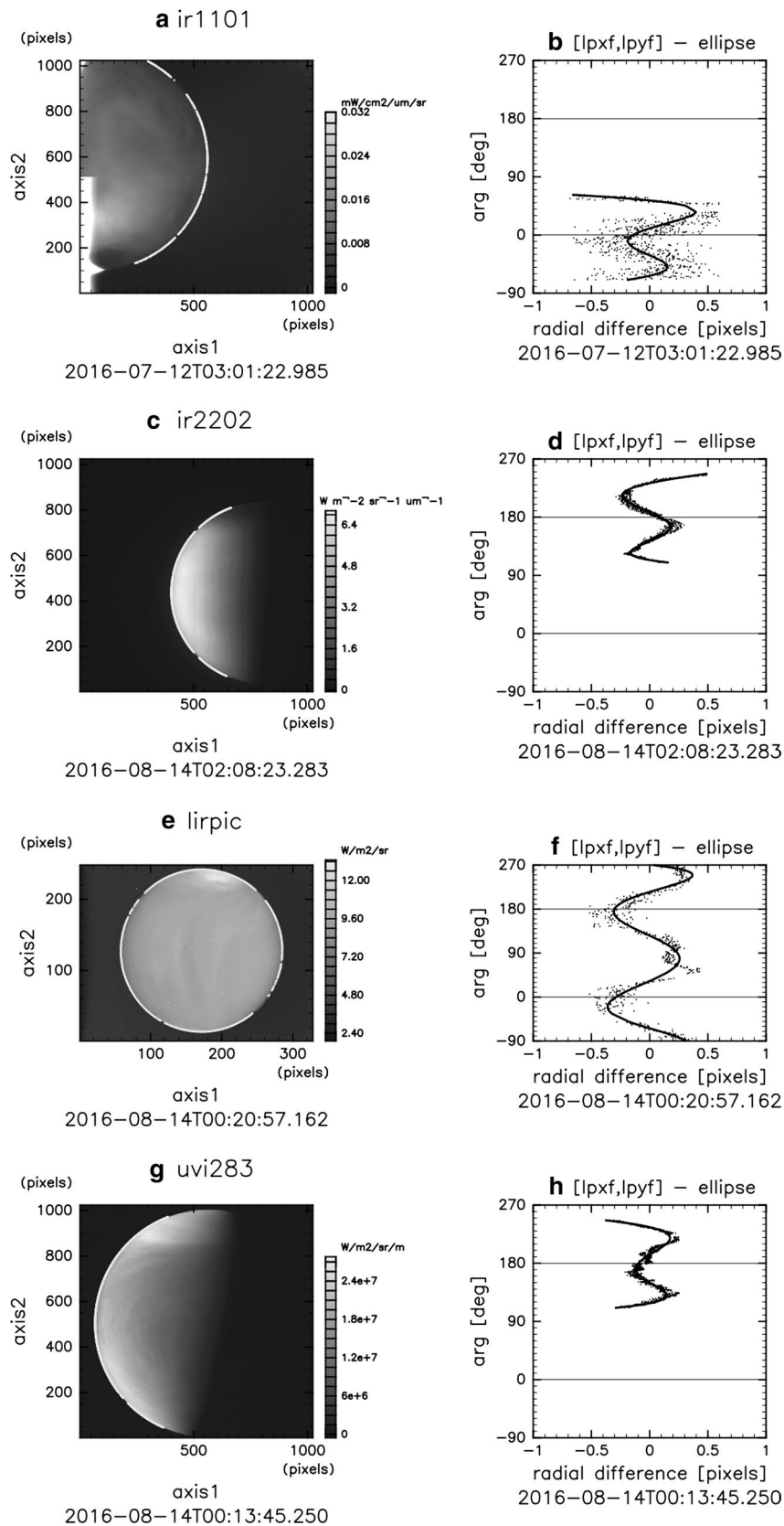
functions obtained by fitting Eq. (4) to the radial residuals of limb points from the ellipse and successfully approximating them. Figure 6a shows the functions derived by fitting Eq. (4) to the radial residuals of limb points detected from 32 images (283-nm) for which the spacecraft–Venus-center distance is less than 1.6×10^4 km. Most of these functions seem to be 3-shape-symmetric about $\theta = 180^\circ$, although they differ in amplitude. Figure 6b–g shows correlations between a and the other coefficients of Eq. (4). It is obvious that coefficients b to g can be approximated by a linear function of a . We obtained similar results for all other wavelengths, though correlations between the coefficients became low, especially for nightside images. Our results imply that the six coefficients (b – g) of Eq. (4) can be roughly determined by the other coefficient (a) for all wavelengths of Akatsuki’s camera. Therefore, if we obtain the average \bar{a} and the standard deviation \hat{a} of the coefficient a , and the standard deviation σ of the residuals from Eq. (4), which cannot be explained by Eq. (4), from several images, we can statistically simulate radial-residual distributions of detected limb points consisting of a sixth-order function and a noise component, as shown in Fig. 5. Table 3 lists \bar{a} , \hat{a} , and σ for each wavelength obtained by fitting Eq. (4) to the radial residuals of the detected limb points from the ellipse determined by fitting (see Additional file 1 for the source images). L and S indicate the cases where the spacecraft is close to and far from the center of Venus, respectively. The average noise component that remains after fitting Eq. (4) to the radial residuals of the detected limb points is small enough to be negligible relative to σ . Although the shape of the sixth-order function is not easily presumed from the values of \bar{a} and \hat{a} listed in Table 3 alone, the large σ of the nightside wavelengths means that limb points tend to disperse in the radial direction in nightside images.

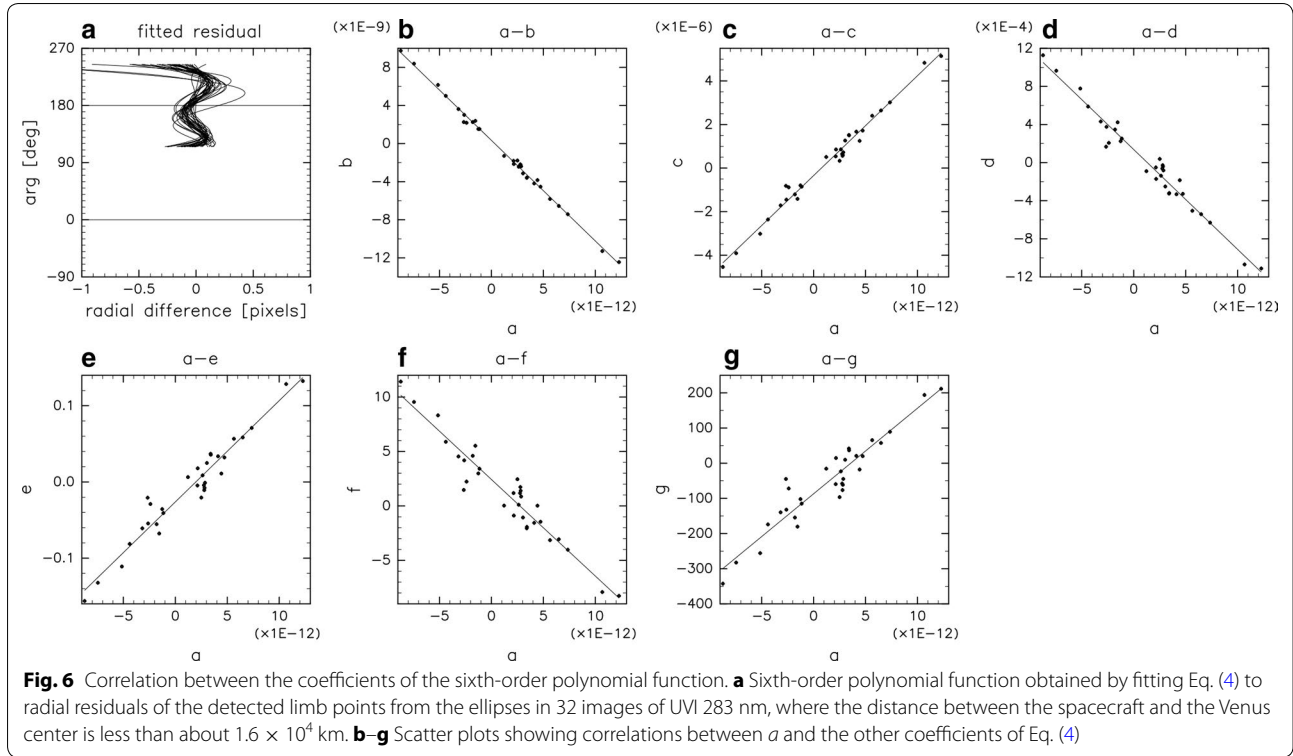
Accuracy of pointing correction

To estimate the accuracy of the pointing correction, we introduce a virtual Venusian disk expressed by an ellipse E , whose center is located on $C(x_{ct}, y_{ct})$, and an elliptical arc E' between the angles θ_1 and θ_2 . The ellipticity and inclination of the semimajor axis of E depend upon $C(x_{ct}, y_{ct})$ and are determined based on the geometry described by Ogohara et al. (2012). Figure 7 shows samples of the true elliptical arcs E' used in the next

(See figure on next page.)

Fig. 5 Observed images, the 3-shape, and the ε -shape. **a, c, e,** and **g** Sample images in the cases where the Venus disk is large (1.01 μm , 2.02 μm , LIR, 283 nm) and **b, d, f,** and **h** the distributions of radial residuals of limb points from the ellipses. White dots in **(a, c, e,** and **g)** indicate detected limb points used for ellipse fitting. The argument of a vector from the ellipse center toward the positive direction of X is 0° and that of each limb point is measured anticlockwise in **(b, d, f,** and **h)**. Solid lines are sixth-order polynomial functions obtained by fitting Eq. (4) to radial residuals of the limb points from the ellipse





subsection to estimate the accuracy of the pointing correction in the Cases L and S, as listed in Table 3. The number of limb points (M) and the range of the elliptical arc $[\theta_1, \theta_2]$ are set based on observations and are listed in Table 4. The elliptical arc E' and the value M for the nightside wavelengths are short and small, respectively, because limb points are not detected at high latitudes, which are much darker than the mid-latitudes in these bands. The size of ellipse E is common for all cameras except for LIR, where it is smaller. By contrast, M for LIR is not much smaller than that for the other cameras because LIR captures the whole Venusian disk and E' is identical to E . Table 4 also shows the true sub-spacecraft point (x_{SSCt}, y_{SSCt}) assumed for the test and the angle, θ_{Vt} , between the boresight vector and the true \vec{L}_V , as calculated from true ellipse E , based on Ogohara et al. (2012).

We add the radial residuals, r , and Gaussian noise, ε , generated from the parameters listed in Table 3 to the true limb points located on the true elliptical arc, E' . We use $\mathbf{d}_1, \mathbf{d}_2, \dots, \mathbf{d}_M$ to denote the position vectors of M points that divide E' equally into $M - 1$ parts and randomly generate a position vector, \mathbf{q}_j , of the j th pseudo-limb point as follows:

$$\mathbf{q}_j = \frac{\mathbf{d}_j - \mathbf{c}}{|\mathbf{d}_j - \mathbf{c}|} (r(\theta_j) + \varepsilon) + \mathbf{d}_j, \quad (5)$$

$$\theta_j = \theta_1 + \frac{\theta_2 - \theta_1}{M - 1} (j - 1). \quad (6)$$

Here, \mathbf{c} is the position vector of C ; $r(\theta_j)$ is calculated from Eq. (4) if coefficient a is given randomly based on the average and standard deviation listed in Table 3; and ε is also given based on Table 3.

Next, we estimate the sub-spacecraft point (x_{SSCe}, y_{SSCe}) and the angle, θ_{Ve} , between the boresight vector and \vec{L}_V , by fitting an ellipse to M pseudo-limb points expressed by Eqs. (5) and (6) and calculate the differences from their true values, $\Delta x_{SSC} = x_{SSCe} - x_{SSCt}$, $\Delta y_{SSC} = y_{SSCe} - y_{SSCt}$, and $\Delta \theta_V = \theta_{Ve} - \theta_{Vt}$. M pseudo-limb points are generated 1000 times independently using the parameters listed in Table 3. The ensemble average (denoted by an overline) and the ensemble standard deviation (denoted by a hat) of Δx_{SSC} , Δy_{SSC} , and $\Delta \theta_V$ are listed in Table 5.

The absolute values of $\overline{\Delta x_{SSC}}$, $\overline{\Delta y_{SSC}}$, and $\overline{\Delta \theta_V}$ in Cases L and S are comparable to Δx_{SSC} , Δy_{SSC} , and $\Delta \theta_V$, respectively, for dayside wavelengths. Such biases in the sub-spacecraft point associated with ellipse fitting were not recognized in results by Ogohara et al. (2012). The same trials as Ogohara et al. (2012) with $r(\theta) = 0$, in which just the noise component is given randomly, showed that Δx_{SSC} , Δy_{SSC} , and $\Delta \theta_V$ were very close to zero.

Therefore, these biases result from the 3- or ε -shape of the limb-point distributions and the small standard deviation in the noise component. What may be a problem for practical use are variances in Δx_{SSC} , Δy_{SSC} , and $\Delta \theta_V$, because we can rotate \vec{L}_V in addition when calculating the radiance on each longitude–latitude grid, such that these biases vanish. Differences $\overline{\Delta x_{SSC}}$ and $\overline{\Delta y_{SSC}}$ are smaller than 0.1 and 0.01, respectively, in the dayside Cases L and S. Difference $\overline{\Delta x_{SSC}}$ is larger than $\overline{\Delta y_{SSC}}$, since the limb is assumed to be located on the left-hand side of the images ($\theta_1 = 115^\circ, \theta_2 = 245^\circ$). There is not a large difference in $\overline{\Delta \theta_V}$ between Cases L and S. However, the impact of the pointing accuracy upon cloud-feature positions in longitude–latitude coordinates is larger in Case S than in Case L, since the distance between the spacecraft and Venus’s center in Case S is longer than that in Case L. Variations in cloud-feature positions (1σ) are, for example, 5.8×10^{-2} km (UVI 365 nm) and 8.6 km (IR1 0.97 μm) when the spacecraft–cloud-layer distance is 10^4 km. When this distance is 10^5 km, the 1σ values are 3.6×10^{-1} km (UVI 283 nm) and 7.0 km (IR2 2.26 μm). However, it should be noted that the above standard deviations in pointing are estimated under ideal conditions. Users should care about the effects of satellite thermal conditions and uncertainties in the limb altitudes upon the positions of cloud features if, for

example, they are attempting to perform cloud tracking using L3 products (“[Interpretation of the estimated accuracy](#)” section).

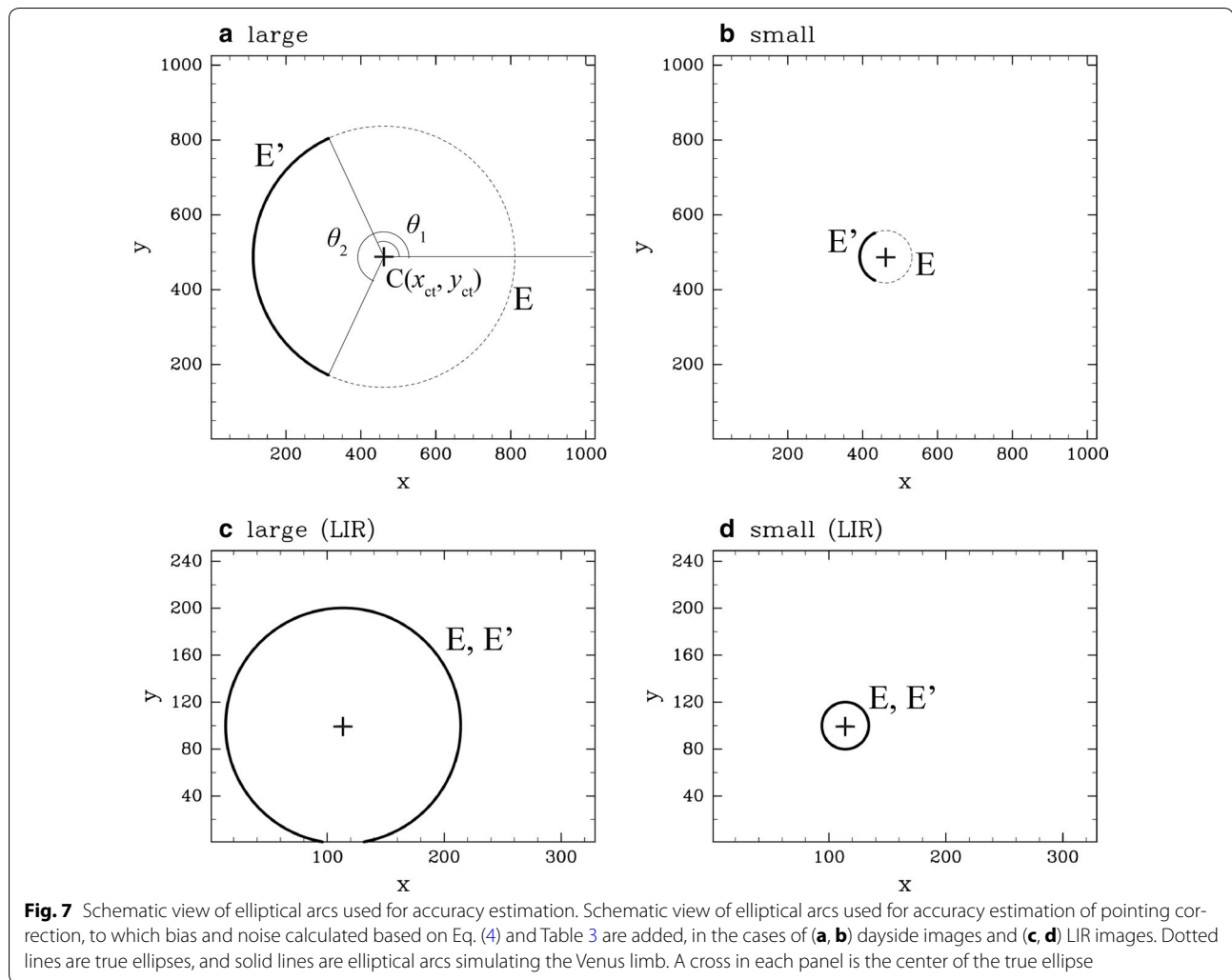
The accuracies of sub-spacecraft-point determination at the nightside wavelengths are markedly worse than those at dayside wavelengths. This is because the length of the limb tends to be short and the detected limb points tend to be dispersed, due to low contrast between space and Venus (especially at high latitudes). There is no IR1 nightside image corresponding to Case S in which the spacecraft is far from Venus. In most nightside images, $\overline{\Delta x_{SSC}}$, $\overline{\Delta y_{SSC}}$, $\overline{\Delta \theta_V}$, and $\overline{\Delta \theta_V}$ range from $O(10^{-3})$ to $O(10^{-1})$, but they are $O(10^0)$ at some wavelengths. The ellipse fitting of IR1 0.97- μm images in Case L resulted in completely incorrect ellipses in some of the 1000 time trials conducted. It is likely that $\overline{\Delta x_{SSC}}$ and $\overline{\Delta y_{SSC}}$ seem to be large due to the small number of outliers. Note that the values for IR1 0.9- μm (nightside) in Case L listed in Table 5 are unreliable because only four observed images are available for the derivation of \bar{a} , \hat{a} , and σ .

The accuracy of sub-spacecraft-point determination using images taken by LIR with an arc angle of 360° is much better than those obtained by the other instruments. However, it is not always better than that of the other cameras if it is measured in $\overline{\Delta \theta_V}$, $\overline{\Delta \theta_V}$ because of the low spatial resolution of LIR. The difference in LIR

Table 3 Parameters calculated from detected limb points in each wavelength

Case	Instrument	Wavelength (μm)	Day/night	\bar{a}	\hat{a}	σ
L	ir1	0.97	Night	$-4.82\text{E}-11$	$8.82\text{E}-11$	$8.22\text{E}-01$
	ir1	0.9	Day	$-1.23\text{E}-11$	$1.98\text{E}-11$	$4.29\text{E}-02$
	ir1	0.9	Night	$-4.35\text{E}-11$	$8.05\text{E}-11$	$9.51\text{E}-01$
	ir1	1.01	Night	$4.46\text{E}-12$	$4.03\text{E}-11$	$3.04\text{E}-01$
	ir2	1.74	Night	$-9.22\text{E}-12$	$2.94\text{E}-11$	$1.62\text{E}-01$
	ir2	2.02	Day	$-3.12\text{E}-12$	$2.29\text{E}-11$	$8.56\text{E}-02$
	ir2	2.26	Night	$-8.83\text{E}-11$	$1.15\text{E}-10$	$3.51\text{E}-01$
	ir2	2.32	Night	$-9.06\text{E}-11$	$9.38\text{E}-11$	$3.84\text{E}-01$
	lir		Both	$-1.68\text{E}-13$	$6.11\text{E}-14$	$8.32\text{E}-02$
	uvi	0.283	Day	$1.41\text{E}-12$	$4.72\text{E}-12$	$2.94\text{E}-02$
	uvi	0.365	Day	$1.44\text{E}-12$	$5.06\text{E}-12$	$3.63\text{E}-02$
	S	ir1	0.9	Day	$4.27\text{E}-12$	$3.93\text{E}-12$
ir2		1.74	Night	$-2.03\text{E}-11$	$6.07\text{E}-11$	$1.73\text{E}-01$
ir2		2.02	Day	$4.06\text{E}-13$	$8.25\text{E}-12$	$4.62\text{E}-02$
ir2		2.26	Night	$-5.20\text{E}-11$	$1.17\text{E}-10$	$2.50\text{E}-01$
ir2		2.32	Night	$-2.10\text{E}-11$	$1.07\text{E}-10$	$3.27\text{E}-01$
lir			Both	$-1.32\text{E}-13$	$3.48\text{E}-14$	$5.45\text{E}-02$
uvi		0.283	Day	$1.32\text{E}-12$	$6.20\text{E}-12$	$2.97\text{E}-02$
uvi		0.365	Day	$-5.36\text{E}-14$	$7.62\text{E}-12$	$4.53\text{E}-02$

The average \bar{a} and standard deviation \hat{a} in coefficient a , and the standard deviation σ in residuals from Eq. (4). Coefficient a and residuals from Eq. (4) are derived by fitting Eq. (4) to radial residuals of limb points detected in images listed in Additional file 1 from the ellipses. Cases L and S mean the cases where the distance between the spacecraft and the Venus center is shorter than 1.6×10^4 km and longer than 3.5×10^4 km, respectively



from the other cameras listed in Table 5 shows that $|\overline{\Delta y_{SSC}}|$ is larger than $|\overline{\Delta x_{SSC}}|$. This is probably because the distributions of detected limb points tend to be longer in the Y-direction than the true ellipse.

Interpretation of the estimated accuracy

It is not clear what gives rise to the 3-shape and the ε -shape, and their reasons are beyond the scope of this study. However, we can determine the sub-spacecraft point and L_V at the accuracies listed in Table 5, if the limb points follow such radial-residual distributions for any reason. Accuracies $\overline{\Delta x_{SSC}}$, $\overline{\Delta y_{SSC}}$ and $\overline{\Delta x_{SSC}}$, $\overline{\Delta y_{SSC}}$ listed in Table 5 range from $O(10^{-3})$ to $O(10^{-1})$ at most wavelengths. They are the accuracies of an algorithm that derives an optimal ellipse approximating the distribution of given points. In this study, we detect limb points by fitting a tanh function to the radiance distributions in the X- or Y-directions and assume that these limb points are located at a cloud altitude that depends upon wavelength.

However, it is not clear whether one-dimensional distributions of radiance can be expressed by a tanh function, or whether it would be reasonable (or acceptable) to assume constant cloud-top altitudes along local times and latitudes. It remains unclear how the cloud altitudes depend upon latitude and local time at each wavelength. At present, we do not know the typical profile of radiance around the limb or where the profile of the limb should be defined. The positional accuracy of the limb points is reasonably lower than that listed in Table 5. Therefore, the pointing-correction accuracies listed in Table 5 should be understood to be the most optimistic values.

Figure 8 shows sequential longitude–latitude maps (nightside) taken at a 2.26- μm wavelength by the IR2 camera. A feature (Feature A) seen around 115°W, 10°S in Fig. 8a is not shifted in Fig. 8b–d (meaning that Feature A is moving westward at 80 m s^{-1}). However, Feature A suddenly jumps westward by about 2° in Fig. 8e. Because the time interval is 2 h, this jump corresponds to about

Table 4 Parameters of the true elliptical arcs used for investigating the accuracy of pointing correction

Case	Instrument	Wavelength (μm)	Day/night	M	θ_1 (deg)	θ_2 (deg)	x_{SSCt} (pix)	y_{SSCt} (pix)	θ_{vt} (rad)
L	ir1	0.97	Night	606	-55	55	462	488	0.011
	ir1	0.9	Day	660	115	245	462	488	0.011
	ir1	0.9	Night	606	-55	55	462	488	0.011
	ir1	1.01	Night	606	-55	55	462	488	0.011
	ir2	1.74	Night	606	-55	55	462	488	0.011
	ir2	2.02	Day	660	115	245	462	488	0.011
	ir2	2.26	Night	606	-55	55	462	488	0.011
	ir2	2.32	Night	606	-55	55	462	488	0.011
	lir		Both	400	-90	270	114	100	0.049
	uvi	0.283	Day	660	115	245	462	488	0.012
S	uvi	0.365	Day	660	115	245	462	488	0.012
	ir1	0.9	Day	132	115	245	462	488	0.011
	ir2	1.74	Night	107	-55	55	462	488	0.011
	ir2	2.02	Day	132	115	245	462	488	0.011
	ir2	2.26	Night	107	-55	55	462	488	0.011
	ir2	2.32	Night	107	-55	55	462	488	0.011
	lir		Both	80	-90	270	114	100	0.049
	uvi	0.283	Day	132	115	245	462	488	0.012
	uvi	0.365	Day	132	115	245	462	488	0.012

M , θ_1 , and θ_2 are roughly determined from images listed in Additional file 1. x_{SSCt} , y_{SSCt} , and θ_{vt} are derived from Ogohara et al. (2012)

Table 5 Results of the accuracy evaluation

Case	Instrument	Wavelength (μm)	Day/Night	$\overline{\Delta x_{SSC}}$ (pixels)	$\widehat{\Delta x_{SSC}}$ (pix)	$\overline{\Delta y_{SSC}}$ (pix)	$\widehat{\Delta y_{SSC}}$ (pix)	$\overline{\theta_v}$ (rad)	$\widehat{\theta_v}$ (rad)
L	IR1	0.97	Night	6.2E-02	2.0E+00	-1.5E+00	6.7E+00	1.8E-04	8.6E-04
		0.9	Day	-8.3E-02	6.7E-02	-1.2E-02	1.2E-02	1.6E-05	1.3E-05
		0.9	Night	-1.5E+00	1.1E+00	-1.4E-01	2.3E+00	2.9E-04	2.6E-04
		1.01	Night	-7.1E-01	3.7E-01	-7.7E-03	2.8E-02	1.3E-04	6.7E-05
	IR2	1.74	Night	-1.5E-01	1.2E-01	-1.5E-03	5.5E-02	2.8E-05	1.8E-05
		2.02	Day	-9.8E-02	4.4E-02	-9.4E-03	1.4E-02	1.8E-05	7.0E-06
		2.26	Night	-3.6E-01	1.2E-01	-1.0E-01	1.6E-01	7.4E-05	2.8E-05
		2.32	Night	-1.7E-01	4.4E-01	-1.2E-01	1.1E-01	4.1E-05	7.1E-05
	LIR		Both	-5.8E-03	8.4E-03	3.5E-02	8.0E-03	-8.8E-06	8.2E-06
		UVI	0.283	Day	5.2E-02	4.0E-02	-9.1E-03	4.3E-03	-8.9E-06
S	UVI	0.365	Day	8.5E-02	3.7E-02	-3.1E-03	1.1E-02	-1.5E-05	5.8E-06
		IR1	0.9	Day	6.3E-03	2.3E-02	3.6E-03	7.0E-03	-1.5E-06
	IR2	1.74	Night	-7.3E-02	1.7E-01	-6.4E-03	3.5E-02	1.4E-05	3.1E-05
		2.02	Day	-1.8E-02	3.4E-02	8.0E-04	1.3E-02	3.1E-06	5.5E-06
		2.26	Night	-1.9E-01	4.1E-01	-2.0E-02	7.0E-02	3.6E-05	7.0E-05
		2.32	Night	-2.5E-01	3.0E-01	7.9E-03	6.7E-02	4.3E-05	5.5E-05
	LIR		Both	7.0E-03	9.5E-03	5.8E-02	1.8E-02	-2.8E-05	1.0E-05
	UVI	0.283	Day	2.8E-03	1.9E-02	-1.5E-02	7.7E-03	8.5E-07	3.6E-06
		0.365	Day	2.8E-02	3.0E-02	-1.2E-02	7.9E-03	-4.1E-06	5.5E-06

The average and the standard deviation in Δx_{SSC} , Δy_{SSC} , and $\Delta \theta_v$ for each wavelength resulting from 1000 time trials of the ellipse fitting

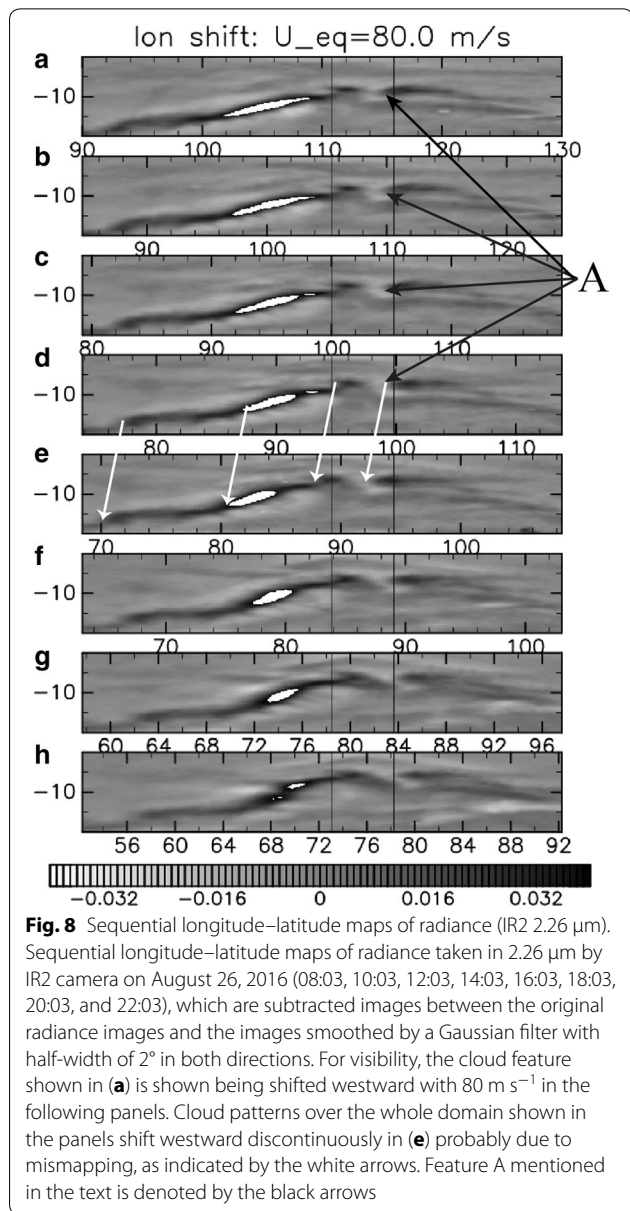
a 30-m s^{-1} increase in the easterly wind speed. Furthermore, the westward jump is not local but is seen over the whole domain, as shown by the white arrows in Fig. 8. The radius of Venus in the original IR2 images around the time when the jump occurred was approximately 120 pixels, so the jump of 2° , which was observed near the sub-spacecraft point, corresponds to an erroneous shift in the pointing correction by ~ 4 pixels. This was the worst case, but jumps larger than $\sim 20\text{ m s}^{-1}$ were found in about one-third of all IR2 $2.26\text{ }\mu\text{m}$ cases where cloud tracking was successfully performed during the period from 2016-07-11 to 2016-09-06 (see Ikegawa and Horinouchi 2016; Horinouchi et al. 2017a, b for our cloud-tracking method). This indicates that, in the nightside cases, the

actual error of the pointing correction can become $O(1)$ pixels, which is much greater than the $O(10^{-1})$ -pixel error indicated in Table 5. We are still investigating the reason for this discrepancy, but we suspect that it is related to the nature of the nightside radiance at $\sim 2\text{ }\mu\text{m}$, which is often very dark and obscure at the limb. Overall, we strongly recommend that L3-product users estimate the mapping accuracy for their particular topics (e.g., cloud tracking) by themselves. One way to do so is to compare cloud-tracking results from multiple combinations of successively obtained images. See the online supplement (“Methods” section) of Horinouchi et al. (2017b) for more details. Note that those authors used a different algorithm to correct pointing and succeeded in reducing the jumps. However, the performance of their algorithm for dayside and IR1-nightside images is unknown, so we did not use it to produce the Level-3 data. We plan to improve the fitting for nightside images in the Level-3 pipeline in the future. Unlike nightside images, discontinuities in cloud-feature positions rarely occur in dayside sequences. Comparing Figs. 2 and 4, the accuracy of longitude–latitude mapping (i.e., the pointing accuracy) has clearly been improved by ellipse fitting. The algorithm whose performance has been investigated by this study enables a variety of studies on the Venusian atmosphere.

Summary

We developed a data-processing pipeline to generate Akatsuki imaging data from the UVI, IR1, IR2, and LIR cameras. This pipeline has multiple levels, which we call Levels 1a, 1b, 2b, and 3. Levels 1 (1a and 1b) and 2 (2b) consist of uncalibrated and calibrated data (radiance for UVI, IR1, and IR2, and brightness temperature for LIR), respectively. Level-1b data are based on the data from Level 1a by adding geometry information such as the phase, incidence, and emission angles. The data for Levels 1a, 1b, and 2b are stored in the FITS format, commonly used for planetary science. Level-3 data are global maps on the regular longitude–latitude grids, which are produced based on Level-2b data. The errors in the navigation data and the instrument alignment, which cannot be neglected when producing Level-3 data, are corrected by an improved limb-fitting technique in which the pointing of the boresight vector is corrected by fitting an ellipse to the Venusian limb. Level-3 data are stored in the NetCDF format commonly used for atmospheric science.

The accuracy of pointing correction has been statistically estimated. The result shows that the algorithm we developed and used for Level-3 data works well; the uncertainties in the sub-spacecraft point are about $O(10^{-2}\text{--}10^{-1})$ pixels. It is expected that the Level-3 data will be useful for deriving the CMVs accurately, except for some of the nightside images. The pointing-correction



method developed for the Akatsuki data pipeline can be applied to the Venusian images obtained from previous missions. It is noted, however, that the present error estimation of the pointing correction is based on assumed ideal conditions. Therefore, we must pay attention to various factors such as the thermal conditions of the satellite and/or the uncertainty in the assumed cloud altitudes, which could affect the pointing correction. We hope that the Akatsuki public data will be widely used for Venusian atmospheric science.

Additional file

Additional file 1. List of files used for accuracy estimation of pointing correction. List of image files used for calculating parameters \bar{a} , \hat{a} and σ . This is also used for roughly estimating θ_1 and θ_2 . Names of the files displayed in this Additional file 1 may not be exactly identical to those stored in the publication sites, where the data files are released to the public. However, users can find the file uniquely because the observation date is included in each file name.

Abbreviations

CCD: charge-coupled device; CMV: cloud-motion vector; DARTS: the Data Archive and Transmission System; DE: digital electronics; DR: data recorder; FITS: Flexible Image Transport System; FOV: field of view; HDU: Header Data Unit; HLS: hyperaccurate least squares; IFOV: instantaneous field of view; IR1: infrared 1- μ m camera; IR2: infrared 2- μ m camera; JAXA: Japan Aerospace Exploration Agency; JPEG: Joint Photographic Experts Group; JPL: Jet Propulsion Laboratory; L1a: Level 1a; L1b: Level 1b; L2a: Level 2a; L2b: Level 2b; L3: Level 3; L3x: Level 3x; LAC: Lightning and Airglow Camera; LIR: long-wave infrared camera; NASA: National Aeronautics and Space Administration; NetCDF: Network Common Data Format; SIRIUS: Scientific Information Retrieval and Integrated Utilization System; TI: time indicator; UVI: ultraviolet imager; UV: ultraviolet; VCO: Venus Climate Orbiter; VMC: Venus Monitoring Camera.

Authors' contributions

KO, MT, HK, NS, MY, SM, AY, TK, and TH developed the algorithm. KO and MT were involved in accuracy estimation. TH and SM were involved in cloud tracking. NI, SO, TS, TMS, AY, SW, MY, MT, TF, TI, MS, MF, TS, and SK developed and calibrated an instrument. SM, GLH, and YY were involved in data processing and archiving inside JAXA. TI, TS, TMS, SO, AY, MY, TF, MS, KO, KS, HA, and HK operated the spacecraft. TI and Y-JL developed the observation planning. CH and NI calculated the orbit. MN, TA, NI, and TS were involved in management of the project. All authors read and approved the final manuscript.

Author details

¹ School of Engineering, University of Shiga Prefecture, 2500, Hassaka, Hikone, Shiga 522-8533, Japan. ² Division of Science, Kyoto Sangyo University, Kamigamo Motoyama, Kita-ku, Kyoto 603-8555, Japan. ³ Institute of Space and Astronautical Science, Japan Aerospace Exploration Agency, 3-1-1 Yoshinodai, Chuo-ku, Sagami-hara, Kanagawa 252-5210, Japan. ⁴ Faculty of Environmental Earth Science, Hokkaido University, N10W5, Sapporo, Hokkaido 060-0810, Japan. ⁵ Planetary Exploration Research Center, Chiba Institute of Technology, 2-17-1 Tsudanuma, Narashino, Chiba 275-0016, Japan. ⁶ Artificial Intelligence Research Center, National Institute of Advanced Industrial Science and Technology, 2-3-26 Aomi, Koto-ku, Tokyo 135-0064, Japan. ⁷ Department of Earth Science, Okayama University, 3-1-1 Tsushima-naka, Kita, Okayama 700-8530, Japan. ⁸ Graduate School of Frontier Sciences, University of Tokyo, 5-1-5 Kashiwanoha, Kashiwa, Chiba 277-8561, Japan. ⁹ Institute of Space and Astronautical Science, Japan Aerospace Exploration Agency, 3-1-1 Yoshinodai, Chuo-ku, Sagami-hara, Kanagawa 252-5210, Japan. ¹⁰ Department of Planetology/Center for Planetary Science, Kobe University, 7-1-48, Minamimachi, Minatogima, Chuo-ku, Kobe 650-0047, Japan. ¹¹ School of Computer Science and Engineering, The University of Aizu, Aizuwakamatsu, Fukushima 965-8580, Japan. ¹² Natural Science Division, Tokyo Gakugei University, 4-1-1 Nukui Kitamachi,

Koganei, Tokyo, Japan. ¹³ Department of Physics, Rikkyo University, 3-34-1 Nishi-Ikebukuro, Toshima-ku, Tokyo 171-8501, Japan. ¹⁴ Hokkaido Information University, Ebetsu, Hokkaido 069-8585, Japan. ¹⁵ School of Commerce, Senshu University, 2-1-1, Higashimita, Tama-ku, Kawasaki, Kanagawa, Japan. ¹⁶ Omori Medical Center, Toho University, 6-11-1 Omori-Nishi, Ota-ku, Tokyo 143-8541, Japan. ¹⁷ Planetary Plasma and Atmospheric Research Center, Graduate School of Science, Tohoku University, Aramaki-aza-aoba, Aoba, Sendai 980-8578, Japan. ¹⁸ Department of Information Engineering, National Institute of Technology, Matsue College, 14-4 Nishi-Ikuma, Matsue, Shimane 690-8518, Japan. ¹⁹ Division of Science, Kyoto Sangyo University, Kamigamo Motoyama, Kita-ku, Kyoto 603-8555, Japan. ²⁰ 4-18-9 Akatsutsumi, Setagaya-ku, Tokyo 156-0044, Japan.

Acknowledgements

The authors thank all the members of the Akatsuki project team for their remarkable support in developing and operating the spacecraft and processing data on the ground. This study is partially supported by JSPS KENHI 16H02231 and 16H02225.

Competing interests

The authors declare that they have no competing interests.

Consent for publication

Not applicable.

Availability of data and materials

L2 and L3 data and the SPICE kernels used in this study are the internal release version v20170601 of the products. However, they will be released to the public through the JAXA's data publication site <http://darts.isas.jaxa.jp/planet/project/akatsuki/>.

Ethics approval and consent to participation

Not applicable.

Funding

This study is partially supported by JSPS KAKENHI 16H02231 and 16H02225.

Publisher's Note

Springer Nature remains neutral with regard to jurisdictional claims in published maps and institutional affiliations.

Received: 28 July 2017 Accepted: 27 November 2017

Published online: 12 December 2017

References

- Del Genio AD, Rossow WB (1990) Planetary-scale waves and the cyclic nature of cloud top dynamics on Venus. *J Atmos Sci* 47(3):293–318
- Dickinson RE (1969) The steady circulation of a non-rotating, viscous, heat-conducting atmosphere. *J Atmos Sci* 26:1199–1214
- Fels SB, Lindzen R (1974) The interaction of thermally excited gravity waves with mean flows. *Geophys Fluid Dyn* 6(2):149–191
- Garcia RF, Drossart P, Piccioni G, López-Valverde M, Occhipinti G (2009) Gravity waves in the upper atmosphere of Venus revealed by CO₂ nonlocal thermodynamic equilibrium emissions. *J Geophys Res* 114:E00B32. <https://doi.org/10.1029/2008JE003073>
- Gierasch PJ (1975) Meridional circulation and the maintenance of the Venus atmospheric rotation. *J Atmos Sci* 32(6):1038–1044
- Hinson D, Jenkins J (1995) Magellan radio occultation measurements of atmospheric waves on Venus. *Icarus* 114(2):310–327
- Horinouchi T, Kouyama SMT, Ogohara K, Yamazaki A, Yamada M, Watanabe S (2017a) Image velocimetry for clouds with relaxation labeling based on deformation consistency. *Meas Sci Technol*. <https://doi.org/10.1088/1361-6501/aa695c>
- Horinouchi T et al (2017b) Equatorial jet in the lower to middle cloud layer of Venus revealed by Akatsuki. *Nat Geosci* 10:646–651. <https://doi.org/10.1038/ngeo3016>

- Ikegawa S, Horinouchi T (2016) Improved automatic estimation of winds at the cloud top of Venus using superposition of cross-correlation surfaces. *Icarus* 271:98–119
- Imamura T, Hashimoto GL (2001) Microphysics of Venusian clouds in rising tropical air. *J Atmos Sci* 58(23):3597–3612
- Ishii N, Yamakawa H, Sawai S, Shida M, Hashimoto T, Nakamura M, Imamura T, Abe T, Oyama K, Nakatani I (2004) Current status of the PLANET-C Venus orbiter design. *Adv Space Res* 34(8):1668–1672. <https://doi.org/10.1016/j.asr.2004.07.006>
- Iwamoto Y, Rangarajan P, Kanatani K (2009) Ellipse fitting by hyperaccurate least squares. IPSJ SIG technical report, 2009-CVIM-168, vol 14, pp 1–8 (**in Japanese**)
- Kouyama T, Imamura T, Nakamura M, Satoh T, Futaana Y (2013) Long-term variation in the cloud-tracked zonal velocities at the cloud top of Venus deduced from Venus Express VMC images. *J Geophys Res Planets* 118(1):37–46
- Kouyama T, Imamura T, Nakamura M, Satoh T, Futaana Y (2015) Vertical propagation of planetary-scale waves in variable background winds in the upper cloud region of Venus. *Icarus* 248:560–568
- Krasnopolsky VA, Pollack JB (1994) H₂O–H₂SO₄ system in Venus' clouds and OCS, CO, and H₂SO₄ profiles in Venus' troposphere. *Icarus* 109(1):58–78
- Lee YJ, Imamura T, Schroeder SE, Marcq E (2015) Long-term variations of the UV contrast on Venus observed by the Venus Monitoring Camera on board Venus Express. *Icarus* 253:1–15. <https://doi.org/10.1016/j.icarus.2015.02.015>
- Machado P, Widemann T, Peralta J, Gonçalves R, Donati J-F, Luz D (2017) Venus cloud-tracked and Doppler velocimetry winds from CFHT/ESPaDONs and Venus Express/VIRTIS in April 2014. *Icarus* 285:8–26
- Matsuda Y (1980) Dynamics of the four-day circulation. *J Meteorol Soc Jpn* 58(6):443–470
- Moroz et al (1985) Solar and thermal radiation in the Venus atmosphere. *Adv Space Res* 5(11):197–232
- Nakamura M et al (2011) Overview of Venus orbiter, Akatsuki. *Earth Planet Space* 63:443–457. <https://doi.org/10.5047/eps.2011.02.009>
- Nakamura M et al (2016) AKATSUKI returns to Venus. *Earth Planets Space* 68:75. <https://doi.org/10.1186/s40623-016-0457-6>
- Ogohara K et al (2012) Automated cloud tracking system for the Akatsuki Venus Climate Orbiter data. *Icarus* 217:661–668. <https://doi.org/10.1016/j.icarus.2011.05.017>
- Peralta J, Hueso R, Sanchez-Lavega A, Piccioni G, Lanciano O, Drossart P (2008) Characterization of mesoscale gravity waves in the upper and lower clouds of Venus from VEX-VIRTIS images. *J Geophys Res Planets* 113:E00B18. <https://doi.org/10.1029/2008JE003185>
- Rosow WB, Del Genio AD, Eichler T (1990) Cloud-tracked winds from Pioneer Venus OCPP images. *J Atmos Sci* 47(17):2053–2084
- Sagdeev RZ, Linkin VM, Blamont JE, Preston RA (1986) The VEGA Venus balloon experiment. *Science* 231:1407–1409
- Schubert G (1983) General circulation and the dynamical state of the Venus atmosphere. In: Hinten D (ed) *Venus*. University of Arizona Press, Tucson, pp 681–765
- Schubert G, Whitehead JA (1969) Moving flame experiment with liquid mercury—possible implications for Venus atmosphere. *Science* 163(3862):71–72
- Schubert G, Covey C, Genio AD, Elson LS, Keating G, Seiff A et al (1980) Structure and circulation of the Venus atmosphere. *J Geophys Res* 85(A13):8007–8025
- Stone Peter H (1968) Some properties of Hadley regimes on rotating and non-rotating planets. *J Atmos Sci* 25:644–657
- Takagi M, Matsuda Y (2006) Dynamical effect of thermal tides in the lower Venus atmosphere. *Geophys Res Lett* 33(13):L13102. <https://doi.org/10.1029/2006GL026168>
- Takagi M, Matsuda Y (2007) Effects of thermal tides on the Venus atmospheric superrotation. *J Geophys Res* 112(D9):D007901. <https://doi.org/10.1029/2006JD007901>
- Taubin G (1991) Estimation of planar curves, surfaces, and nonplanar space-curves defined by implicit equations with applications to edge and range image segmentation. *IEEE Trans Pattern Anal* 13(11):1115–1138
- Thompson R (1970) Venus's general circulation is a merry-go-round. *J Atmos Sci* 27(8):1107–1116
- Yamamoto M, Takahashi M (2004) Dynamics of Venus' superrotation: The eddy momentum transport processes newly found in a GCM. *Geophys Res Lett* 31(9):L09701. <https://doi.org/10.1029/2004GL019518>

Submit your manuscript to a SpringerOpen® journal and benefit from:

- Convenient online submission
- Rigorous peer review
- Open access: articles freely available online
- High visibility within the field
- Retaining the copyright to your article

Submit your next manuscript at ► springeropen.com
